Review of Scientific Instruments

RESEARCH ARTICLE | JULY 16 2024

Wavelength modulation laser-induced fluorescence for plasma characterization

I. Romadanov ; Y. Raitses ; A. Smolyakov

Rev. Sci. Instrum. 95, 073516 (2024)
https://doi.org/10.1063/5.0187687

Review of Scientific Instruments | ARTICLE | pubs.aip.org/aip/rsi

Wavelength modulation laser-induced fluorescence for plasma characterization

Cite as: Rev. Sci. Instrum. 95, 073516 (2024); doi: 10.1063/5.0187687
Submitted: 15 November 2023 • Accepted: 24 June 2024 •
Published Online: 16 July 2024

I. Romadanov,[1,a)] Y. Raitses,[1] and A. Smolyakov[2]

AFFILIATIONS

[1] Princeton Plasma Physics Laboratory, Princeton, New Jersey 08543, USA
[2] Department of Physics and Engineering Physics, University of Saskatchewan, Saskatoon, Saskatchewan S7N 5E2, Canada

[a)] Author to whom correspondence should be addressed: iromada2@pppl.gov

ABSTRACT

Laser-Induced Fluorescence (LIF) spectroscopy is an essential tool for probing ion and atom velocity distribution functions (VDFs) in complex plasmas. VDFs carry information about the kinetic properties of species that is critical for plasma characterization. Accurate interpretation of these functions is challenging due to factors such as multicomponent distributions, broadening effects, and background emissions. Our research investigates the use of Wavelength Modulation (WM) LIF to enhance the sensitivity of VDF measurements. Unlike standard Amplitude Modulation (AM) methods, WM–LIF measures the derivative of the LIF signal. This approach makes variations in VDF shape more pronounced. VDF measurements with WM–LIF were investigated with both numerical modeling and experimental measurements. The developed model enables the generation of both WM and AM signals, facilitating comparative analysis of fitting outcomes. Experiments were conducted in a weakly collisional argon plasma with magnetized electrons and non-magnetized ions. Measurements of the argon ion VDFs employed a narrow-band tunable diode laser, which scanned the $4p^4D_{7/2}$–$3d^4F_{9/2}$ transition centered at 664.553 nm in vacuum. A lock-in amplifier detected the second harmonic WM signal, which was generated by modulating the laser wavelength with an externally controlled piezo-driven mirror of the diode laser. Our findings indicate that the WM–LIF signal is more sensitive to fitting parameters, allowing for better identification of VDF parameters such as the number of distribution components, their temperatures, and velocities. In addition, WM–LIF can serve as an independent method to verify AM measurements and is particularly beneficial in environments with substantial light noise or background emissions, such as those involving thermionic cathodes and reflective surfaces.

I. INTRODUCTION

Laser-Induced Fluorescence (LIF) spectroscopy[1,2] is a diagnostic tool that is used to determine spatially[3,4] and temporally[5,6] resolved measurements of the spectral line profiles of ions or atoms under complex plasma conditions. These conditions commonly occur in laboratory and industrial environments, including plasma processing and electric space propulsion[7–10] applications. In weakly collisional plasmas, the Doppler effect is a primary broadening mechanism of the spectral line profile representing the velocity distribution functions (VDF). This statistical function reveals crucial kinetic properties of plasma, such as temperature and velocities. This paper focuses on LIF measurements in weakly collisional plasmas with non-equilibrium argon ion VDFs (IVDF), excited from metastable levels.

Interpreting VDFs can be ambiguous, especially when dealing with closely located velocity group peaks or partially or entirely overlapped distributions.[11–13] Fluctuations in plasma background emission, measurement noise, and other broadening mechanisms such as the Zeeman[14] or Stark effects[15] further complicate an accurate VDF description. Hence, it is critical to establish a robust methodology for VDF measurements and verification to reduce uncertainty in understanding plasma dynamics.

Derivative spectroscopy,[16] predominantly used in absorption measurements, can be used for quantifying complex absorption features. This technique focuses on the rate of change in the spectral line shape with respect to wavelength, eliminating broad background absorptions and identifying individual features within complex contours. Derivative spectra can be obtained through post-processing of the raw signal or with a combination of electronic and optical methods such as modulation of laser wavelength.[17] Modern diode lasers, with their rapid wavelength, frequency, or shift modulation capabilities,[18,19] offer an appealing option for acquiring derivative spectra through Wavelength Modulation (WM) spectroscopy.[20]

Typically, LIF measurements utilize laser light amplitude modulation (AM), usually performed with a mechanical chopper and acousto- or electro-optic modulators (AOM or EOM), followed by lock-in detection of the pulsed fluorescence signal. WM spectroscopy, often used for enhanced trace species detection,[21] modulates the light's wavelength around a central absorption line at a specific amplitude and frequency. While it is more commonly used for absorption measurements, there have been several studies where fluorescence signals were detected.[22–24] Lock-in detection is used to extract a signal at the n th harmonic of the modulation frequency, which is, under some conditions, proportional to the derivative of the spectral line profile. Advantages of WM spectroscopy include cancellation of the background signal (resulting in a better dynamic range of measurements), sensitivity to VDF shape, and also shifting signals to a higher frequency region, enabling higher frequency modulation compared to AM, reducing 1/f noise, and enhancing the signal-to-noise ratio.[20] It can be noted that other methods have employed the detection of signal harmonics (see Ref. 25). However, the method described therein facilitated the detection of perturbations in velocity distribution functions (VDFs), rather than their derivatives.

It is worth noting that similar WM techniques, when system response to the applied modulation is measured, were applied for electrostatic probe measurements of electron[26] or ion energy distributions.[27] Thus, this approach is fundamental across various fields and applications.

In this work, we employ a WM approach for LIF measurements of VDFs in plasma, using a tunable diode laser to enhance the robustness of VDF analysis. To validate our approach, we carried out modeling studies that underscore the advantages of the derivative-based method and conducted experiments where both AM and WM LIF spectra were collected at various locations within an industrial plasma source (similar to a Bernas source[28]) operating with argon. Numerical simulations showed that the fitting of the WM LIF signal is particularly sensitive to the fitting parameters (e.g., the number of distribution components). This sensitivity results in more reliable fitting, especially in the presence of strong noise. Experimental results corroborated this trend. This shows that WM–LIF can serve as a method to independently verify AM method findings or can be used independently.

This paper is organized as follows: Sec. II introduces derivative spectroscopy and discusses the WM. Section III presents the AM and WM models along with their results. The experimental setup is described in Sec. IV, and the experimental results are detailed in Sec. V. The discussion and comparison of experimental results are provided in Sec. VI. Conclusions are summarized in Sec. VII.

II. REVIEW OF DERIVATIVE AND WM SPECTROSCOPIC TECHNIQUES

A. Derivative spectroscopy

Introduced in the 1950s,[29,30] derivative spectroscopy (DS) is an analytical technique that enhances the resolution and sensitivity of spectroscopic measurements across various applications.[31] In this technique, the spectroscopic data, including absorption or emission spectra, are processed to generate a derivative spectrum. This spectrum represents the rate of change of the original spectrum signal as a function of light wavelength, wavenumber, or frequency.

One of the DS's primary advantages is its ability to enhance line shape analysis by better resolving closely spaced spectral features. In conventional spectra, these features often blend, making it challenging to distinguish individual components. DS addresses this by examining the derivatives of these spectral lines' intensities with respect to the wavelength, enabling a clearer identification of spectral features. The first derivative helps identify the location of a peak, denoted by a zero-crossing point. The second derivative pinpoints the areas of highest curvature in the normal spectrum, thereby improving the resolution of closely spaced spectral features, making overlapping peaks more distinguishable, and improving the detectability of subtle spectral changes. Figure 1(a) shows an example of synthetic Maxwellian VDF (f) for species with zero most probable velocity and a temperature of 0.1 eV. First f' and second f'' derivatives are shown as well. One of the benefits is the cancellation of the background offset. Figure 1(b) provides an example of a synthetic VDF signal resulting from two closely located distributions f_1 and f_2 with parameters as in Fig. 1(a) and most probable velocities of ±300 m/s (converted to the corresponding laser light frequency shift). While the resulting VDF (f) can be misinterpreted as a single Maxwellian VDF, the second derivative makes its true shape immediately obvious. Figure 1(c) illustrates an example of improving the detectability of subtle spectral changes when small, fast Maxwellian distribution f_2 with a temperature of 0.04 eV and a most probable velocity of 950 m/s is completely overlapped by a larger f_1 Maxwellian distribution with a zero most probable velocity and a temperature of 0.22 eV. The second derivative makes the presence of the f_2 distribution clearly identifiable.

Furthermore, DS effectively handles issues such as line shape skewing, baseline drift, and light scattering in conventional spectra. These disturbances often result from variations in background emission or light scatter from the vacuum vessel, optics, or windows. The derivative spectra allow significant cancellation of these effects, improving the description of observed VDFs, for example, Fig. 1(d), where a nonlinear background is added to the Maxwellian distribution with parameters as in Fig. 1(a). It is important to note that if these effects exhibit a strong nonlinear dependency on wavelength, their cancellation could still result in artifacts. For instance, the second derivative will not become zero.

Potential challenges of the DS technique, such as increased noise in higher-order derivatives and the need for precise measurements to avoid wavelength reproducibility errors, can be mitigated by implementing direct measurement techniques rather than post-processing the measured signal. Traditional post-processing, which often involves signal smoothing or fitting, can introduce artifacts into the obtained derivatives. By directly measuring VDF derivatives using techniques such as WM, noise can be effectively suppressed due to the capabilities of lock-in amplifiers.[32] Employing stepwise changes in laser wavelength, rather than scanning, enhances the precision of wavelength measurements. The first and second derivatives typically provide a balance between noise levels and resolution enhancement, highlighting DS's utility in line shape analysis. Further details on this technique can be found in Refs. 16 and 26.

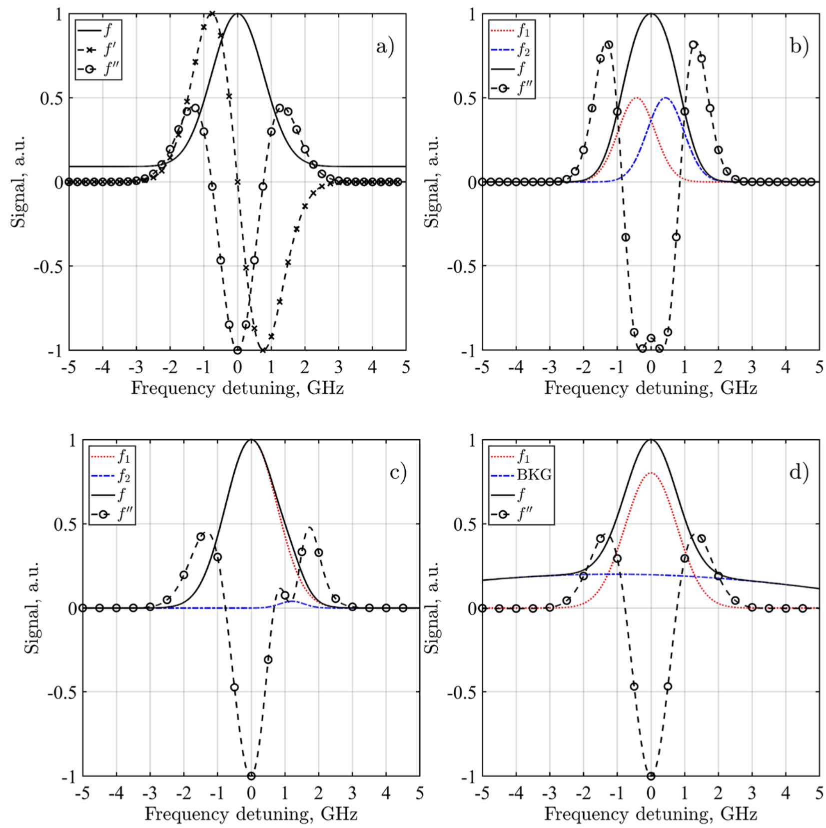

FIG. 1. Illustration of derivative spectroscopy. (a) Single Maxwellian VDF signal (solid black line) and its first (f', dashed line with crosses) and second (f'', dashed line with circles) derivatives. (b) Bi-Maxwellian VDF signal (dotted red and dashed blue lines) with nonzero most probable velocities and its second derivative f'' (dashed line with circles). (c) Bi-Maxwellian VDF signal with a bulk distribution (dotted red) and a smaller faster group (dashed blue) and its second derivative f'' (dashed line with circles). (d) Single Maxwellian VDF (solid black line) signal with a nonlinear (sinusoidal) background (BKG, dashed blue line) and its second derivative f'' (dashed line with circles). Distributions on each subplot are normalized to the maximum of the total distribution (solid black line). Signals and their derivatives were normalized to the maximum absolute value of each curve.

B. WM spectroscopy

WM spectroscopy offers high sensitivity and robustness against background noise, making it suitable for challenging environments characterized by strong turbulence or high pressure and temperature.[33–37] While the principles of WM spectroscopy have been extensively covered in the literature,[17,20] this paper provides just a basic overview, outlined below and schematically illustrated in Fig. 2. The WM technique comprises the following three elements:

1. Wavelength control consists of the scanning and modulation of light's wavelength around a specified center wavelength at a frequency ω_m with a designated modulation amplitude Δ (often referred to as the modulation depth). The capacity to adjust both the modulation amplitude and frequency provides significant flexibility in the measurement process. Typically, modulations are achieved via diode current control, leading to concurrent amplitude modulation. This complicates the analysis of the WM signal, necessitating thorough laser characterization and signal modeling. However, modern diode lasers, which allow for fast (in the kHz range) voltage modulation of grating mount piezo actuators, allow for modulation of the laser wavelength with minimal impact on its amplitude. This facilitates data analysis focused solely on wavelength modulation.
2. The laser light is directed through a test sample, in this instance, plasma. Depending on the measurement type, either light absorption or emitted fluorescence is measured. A suitable detector, such as a photodiode, is employed based on the specific scenario.
3. The detector signal is fed to a lock-in amplifier to extract a certain harmonic of the detector signal at a detection frequency $n\omega_m$, where $n = 1, 2$, and so on, with a bandwidth given by the inverse of the integration time (lock-in amplifier time constant). When the frequency modulation amplitude Δ is much smaller than the width of the absorption profile, the retrieved signal is proportional to the nth harmonic of the cosine series of the absorption profile. It can be shown [see Eq. (B9) in Appendix B of Ref. 20] that nth harmonic of the in-phase

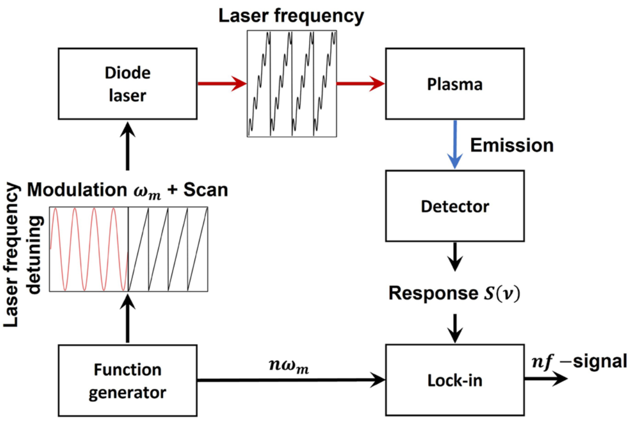

FIG. 2. Schematic representation of WM measurements. The function generator produces overlapping sawtooth and sine waves (ω_m) with distinct frequencies: the Hz range (or lower) for the sawtooth and the kHz range for the sine. These waves drive the diode laser, generating modulated laser light centered on the probed transition's frequency. This modulated light traverses the sample, and the resulting emission is detected. This detected response is then input to the lock-in amplifier, with its reference frequency set to a certain nth harmonic of the sine signal ω_m.

component of the lock-in amplifier output is proportional to the nth derivative of the line shape profile. This is the reason why the WM technique is a DS method.

It is worth mentioning that there's an alternative approach using high-frequency modulation known as frequency modulation (FM) spectroscopy (see Refs. 17 and 38). In general, when modulation is performed at an arbitrary frequency and with an arbitrary amplitude, rigorous signal modeling and laser behavior characterization become important for the correct recovery of the information from the signal. However, this topic is outside the scope of this paper.

III. MODELING OF WM AND AM SIGNALS

This section presents an overview of the foundation for WM and AM signal modeling, with details outlined in Appendixes A and B. The aim is to illustrate that WM signals enable a more reliable extraction of information from measured LIF signals as compared to AM signals, particularly in high-noise environments. Parameters such as the temperature and flow velocities of constituent atomic or ionic groups are typically determined through a fitting procedure applied to experimental data. However, it is crucial to make initial assumptions about the VDF shape, including the expected number of distributions, most probable velocities, and temperatures, to prevent data overfitting. The computation of higher moments of measured distributions (e.g., kurtosis or skewness)[39–41] or other statistical techniques[12,13] can aid in forming these initial assumptions. It is important to note, however, that this analysis can only be performed during post-processing and is significantly influenced by the signal noise and the smoothing or fitting algorithms used for data processing. As demonstrated in Sec. II A, derivatives of distributions can provide similar insights into the VDF shape. WM allows for direct measurements of VDF derivatives, enabling the fitting of the resulting data without additional post-processing.

The model and data processing presented here emulate the steps of a typical LIF measurement. Laser light, characterized by a very narrow linewidth, is tuned around the absorption profile, exciting groups of atoms or ions at varying velocities due to the Doppler effect. These excited species then emit fluorescence light, which is measured by a photodetector device, such as a photomultiplier tube (PMT). To differentiate the fluorescence signal from background emissions (originating from plasma, reflecting walls, filaments, etc.), the signal is typically modulated. This modulation enables the use of homodyne detection[42] measurement systems, such as lock-in amplifiers,[43] known for their ability to extract small amplitude signals from noisy environments. Once the scan across the absorption line is completed, a VDF shape is recovered and subsequently fitted with a function that appropriately describes the assumed distribution. Such a function should correctly describe (temperatures and most probable velocities) all distributions, forming the distribution function.

When analyzing and fitting experimental data, it is essential to consider all effects that could contribute to absorption line broadening. In low-temperature plasmas, several mechanisms can cause broadening, including Zeeman and Stark effects (due to high magnetic or electric fields), the Doppler effect, natural broadening, and hyperfine structures.[44] Doppler broadening, typically the most influential factor, results in a Maxwellian absorption line profile when it originates from the thermal motion of atoms. However, if the medium deviates from thermodynamic equilibrium, the profile may no longer be Maxwellian and can assume various shapes.[10] The hyperfine structure is another crucial factor to consider during profile fitting, with transitions having known hyperfine structures, such as those referenced in Refs. 45 and 46 being preferable.

This study focuses on argon plasma with the most abundant argon isotope under conditions where the Zeeman and Stark effects are negligible. Multimodal distribution, consisting of one or several Maxwellians, is assumed. Such distributions are common in plasma devices with crossed electric and magnetic fields; see Refs. 47–49. Under these circumstances, the Doppler-broadened profile, representing VDF, as a function of laser light frequency ν can be written analytically as follows:[13]

$$f(\nu) = \sum_{k=1}^{N} \frac{c}{\nu_0^k}\left(\frac{M_i}{2\pi k_B T_i^k}\right)^{1/2} \exp\left(-\frac{M_i c^2}{2k_B T_i^k}\frac{\left(\nu-\nu_0^k\right)^2}{\left(\nu_0^k\right)^2}\right), \quad (1)$$

where c is the speed of the light, ν_0 is an LIF transition central frequency, M_i is the mass of the species, k_B is the Boltzmann constant, T_i^k is the kth distribution temperature, ν_0^k is the laser frequency corresponding to the most probable velocity of the of the kth distribution in GHz, and N is the total number of distributions present in the plasma.

Various types of lasers, including solid-state lasers, dye lasers, laser diodes, quantum cascade lasers, and optical parametric oscillators, can adjust their wavelength over a broad range. For high-resolution reconstruction of VDF, continuous wave (CW) laser diodes are preferred due to their extremely narrow bandwidth, typically in the MHz range or below. The laser beam intensity profile, as a function of light frequency, is typically represented by a Lorentzian function as follows[20]:

$$L(\nu, \nu_L) \sim \frac{1}{1 + \frac{(\nu - \nu_L)^2}{\Delta\lambda_L^2}}, \tag{2}$$

where ν_L is the laser central frequency, which can be tuned, and $\Delta\lambda_L$ is the laser linewidth. The equation used to establish the relationship between the laser frequency offset and the velocity is as follows:

$$\Delta\nu = \nu - \nu_0 = \frac{1}{2\pi}\boldsymbol{v} \cdot \boldsymbol{k}, \tag{3}$$

where Δν is the shift in photon frequency from the perspective of the particle, ν_0 is the central laser frequency, $\boldsymbol{v}$ is the particle velocity vector, and $\boldsymbol{k}$ is the photon wavevector.

Typically, the fluorescence signal is excited at a fixed frequency, which is achieved by modulating the laser beam using an oscillator or function generator. This modulated signal serves as the reference input to the lock-in amplifier. The amplifier then identifies the system's response at this reference frequency. In the context of LIF, a response signal $S(\nu)$ represents a fluorescence signal, which is proportional to $\int f(\nu)L(\nu, \nu_L)d\nu$, where the laser central frequency ν_L is scanned across the absorption line. When this signal is measured across a range of light frequencies from ν_1 to ν_2, the output signal from the two-phase lock-in can be expressed as follows:

$$\begin{aligned} X &= \int_{\nu_1}^{\nu_2} S(\nu) \sin\left(2\pi\omega_{ref}\nu(t) + \phi_{ref}\right)d\nu, \\ Y &= \int_{\nu_1}^{\nu_2} S(\nu) \cos\left(2\pi\omega_{ref}\nu(t) + \phi_{ref}\right)d\nu, \end{aligned} \tag{4}$$

where ω_{ref} and ϕ_{ref} represent the frequency and phase of the reference signal, respectively, $\nu(t)$ is the time-dependent laser frequency, and X and Y quantities represent the signal as a vector relative to the lock-in reference oscillator. The X variable is called the "in-phase" component, and Y, the "quadrature" component; for more details, see Ref. 36. By calculating the magnitude (R) of the signal vector as $\sqrt{X^2 + Y^2}$, the phase dependency is eliminated.

For model simplicity, it is assumed that ϕ_{ref} aligns with the phase of the response signal and can thus be omitted. The sweeping range is divided into multiple intervals to recover the Doppler-broadened absorption line (representative of a VDF profile) or its derivatives. The distinction between AM and WM signals is due to different methods of producing the $S(\nu)$ signal. In the case of AM, $L(\nu, \nu_L)$ is a pulse wave function, with amplitude changing between 0 and I. Conversely, in the WM scenario, the amplitude remains constant or oscillates around a certain level, but ν_L varies according to a function described by Eq. (B1). The specifics of both methods, examples of signal shapes, and laser responses to the modulation are described in Appendixes A and B.

The modeling results presented below were obtained by numerically integrating the above equations for AM and WM cases for the following set of parameters, which are relevant to those observed in the experiments with the studied ion source. A bi-Maxwellian singly charged argon ion distribution was assumed, with a bulk distribution at $T_i^1 = 0.22$ eV and zero most probable velocity, and a colder, faster distribution with $T_i^2 = 0.04$ eV and a most probable velocity of 950 m/s. The ratio of peak densities of the two distributions was set at 0.04. These values were used as "ground truth" when evaluating the fitting of the modeled signals. The laser line profile was modeled using Eq. (2) for a linewidth $\Delta\lambda_L = 50$ MHz, which is a typical value for laser diodes. A comparison of the laser linewidths and the distribution is provided in Fig. 3. As illustrated, the laser line is significantly narrower than the VDF shape.

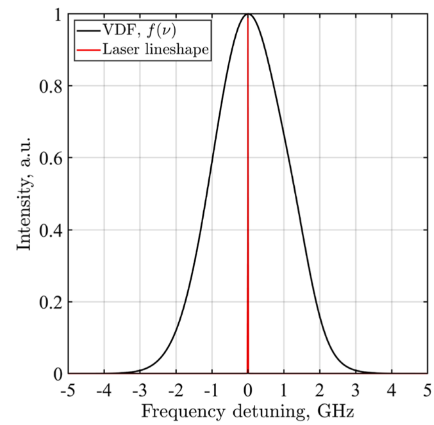

FIG. 3. Laser line shape (red) as compared to the Doppler broadened Ar absorption line.

A. Modeling results

To demonstrate the advantage of the WM technique for the unambiguous extraction of the VDF information from the measured fluorescence signal, Eqs. (A3) and (B2) were numerically solved to obtain lock-in signals with the set of parameters presented earlier. For both cases, the modulation frequency ω_m was set at 15 kHz and the lock-in time constant (integration range) was set at 1 s. Modeling was conducted for AM ($S(\nu, \nu_{AM})$) and WM ($S(\nu, \nu_{WM})$) signals with a noise added to the $f(\nu)$ function [see Eq. (1)]. Noise was modeled as white Gaussian noise with an amplitude of 0.5 at the maximum signal level.

Examples of the AM and WM signals are depicted in Figs. 4(a) and 4(b), respectively. Both signals are normalized to maximum amplitude. The analytical signal was obtained using Eq. (1). The analytical form of the WM signal was obtained as the second derivative of Eq. (1), expressed as follows:

$$f''(\nu) = \frac{2}{\sqrt{\pi}} \sum_{k=1}^{N} \frac{2\left(\nu - \nu_0^k\right)^2 - a_k^2}{a_k^5} \exp\left(-\frac{\left(\nu - \nu_0^k\right)^2}{a_k^2}\right), \tag{5}$$

where $a_k^2 = \frac{\left(\nu_0^k\right)^2}{c^2}\frac{2k_B T_i^k}{M_i}$. The background signal is not accounted for in Eq. (1). However, it is worth noting that the form of Eq. (5) remains unchanged in the presence of a linear background, as the second derivative is zero in such cases.

Typically, when experimental data are processed, the obtained signals are fitted with a single distribution or a sum of several distributions. A similar procedure was done for the modeled signal, and

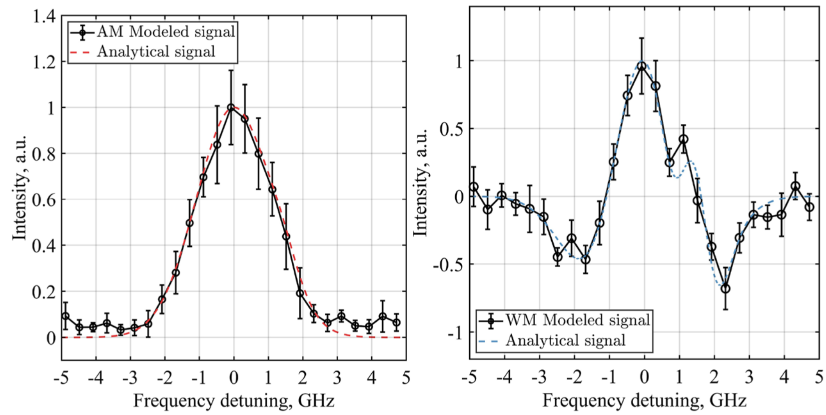

FIG. 4. (a) AM signal from the amplitude modulation model (black solid line) and its analytical form (red dashed line). (b) WM signal from the wavelength modulation model (black solid line) and its analytical form (blue dashed line).

fitting was performed in MATLAB with a weighted nonlinear residual fit function—"lsqnonlin." The goodness of fit (GoF) is evaluated using reduced χ^2_{red}, defined as follows:

$$\chi^2_{red} = \frac{1}{\nu}\sum\frac{\left(f_{obs} - f_{fit}\right)^2}{\sigma^2_{obs}}, \tag{6}$$

where f_{obs} is the observation (the modeled function), f_{fit} is the fitted curve, σ^2_{obs} is the variance, and $\nu = n - m$ is the degree of freedom, where n is the number of points in observation and m is the number of fitted parameters. This procedure is applied to the AM and WM modeled signals, and Eqs. (1) and (5) were used as fitting functions, with the number of distributions (N) varying from 1 to 5. χ^2_{red} was calculated for each case, and χ^2_{red} scores as a function of N are shown in Fig. 5(a). Figure 5(b) shows the estimated most probable velocities and temperatures for two "ground truth" distributions as a function of N.

From Figs. 5(b) and 5(c), it is clear that both AM and WM signals result in an accurate estimation of the most probable velocities and temperatures of "ground truth" distributions. However, from Fig. 5(a), the WM signal results in a minimum of χ^2_{red} at the correct number of distributions, $N = 2$, while the fitting of the AM signal results in a minimum of χ^2_{red} at $N = 3$. Thus, the WM signal provides better sensitivity to the true signal shape.

IV. EXPERIMENTAL SETUP

Experiments were conducted in the experimental setup described in Ref. 50. The setup includes a standard 10″ diameter six-way cross vacuum chamber. A weakly collisional plasma was generated by a low pressure (0.5 mTorr) argon discharge with a hot thermionic cathode and the applied electric and magnetic fields. In the experiments, the magnetic field was varied between 15 and

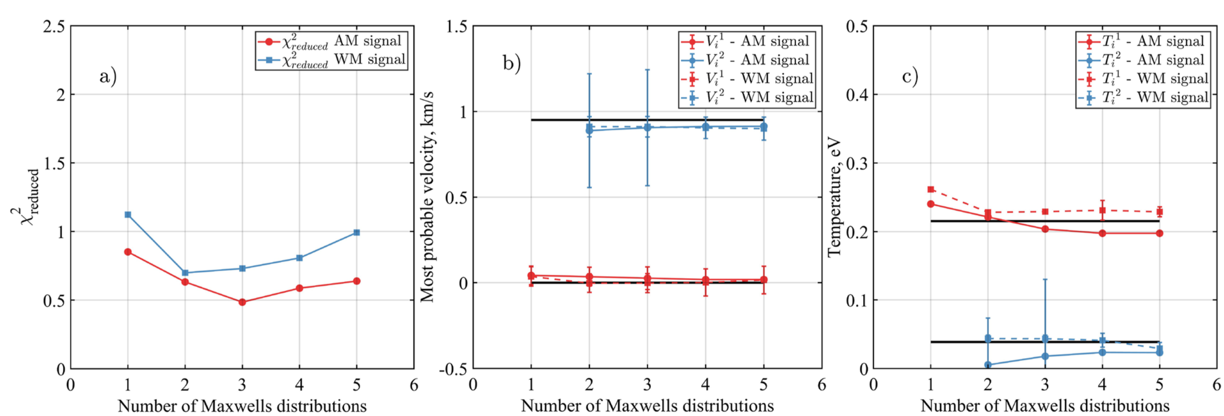

FIG. 5. Fitting results of modeled AM and WM signals with varying numbers of fitted distributions (N = 1–5). (a) $\chi_{red}{}^2$ for AM (red) and WM (blue) signals. (b) Most probable velocity for bulk (V_i^1, red solid for AM and blue solid for WM signals) and fast (V_i^2, red dashed for AM and blue dashed for WM signals); black lines show "ground truth" values. (c) Same as (b) but for temperatures.

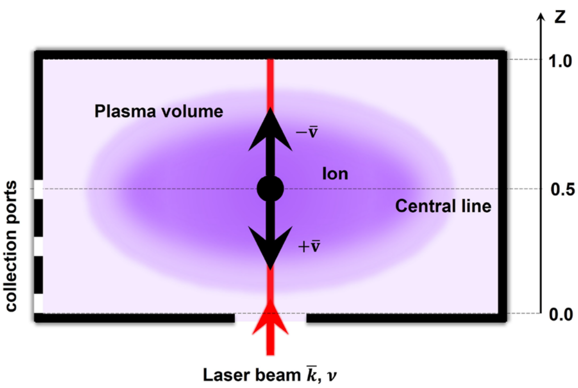

FIG. 6. Schematic of the plasma source illustrates a plasma volume with a diagnostic access opening of <1 cm on the front wall, which is not depicted to scale. The path of the laser beam is indicated in red, while the directions of positive and negative velocities are represented by black arrows.

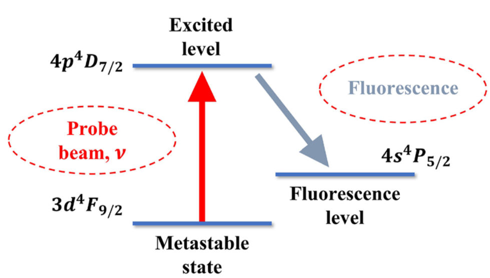

FIG. 7. LIF transition for Ar-II (argon ion).

150 G. The discharge voltage was 50–100 V. The plasma source features a 1 cm diameter opening on the longer front wall (see Fig. 6). A laser beam, with wavevector $\bar{k}$ and frequency ν, is launched through an opening on the front wall. The LIF signal is collected through three additional 3 mm diameter holes on the side wall, which are referred to as central (on the central line), middle, and edge (close to the front surface with the opening). The electron temperature, measured using a sweeping Langmuir probe,[51] was found to be ~5 eV. Given that no other acceleration mechanisms are present in this system, the maximum expected velocity is the Bohm velocity, which is ~3.5 km/s. Therefore, it is anticipated that the observed velocities will fall within the range of ±3.5 km/s.

A. LIF transition

The LIF measurements were conducted by sweeping and simultaneously modulating the frequency of a narrow linewidth, tunable diode laser across the absorption line of an argon ion, which experienced broadening due to the Doppler shift. It was confirmed by previous measurements[50] that the magnetic field used in these experiments does not affect the line broadening. The selected Ar ion transition $3d^4F_{9/2}$–$4p^4D_{7/2}$ at 664.553 nm (in vacuum) and fluorescence at 434.929 nm are depicted in Fig. 7.

B. LIF setup

The LIF system, shown in Fig. 8, is built around a Toptica DLC DL PRO 670 single-mode tunable diode laser (TDL). This Littrow-type grating-stabilized external cavity diode laser offers a coarse tuning range from 660 to 673 nm and a mode-hop free range up to 20 GHz. Depending on the wavelength, the output power reaches a peak of ~23 mW. The system maintains a short-term linewidth stability of 600 kHz over 5 μs. The emitted beam, which is elliptical in shape, is Gaussian with a typical size of around 3 mm.

The laser wavelength is controlled by simultaneous scanning and applying a sinusoidal modulation to the voltage directed at the piezo actuator from a signal generator. When modulation is applied to the piezo actuator, the laser power remains constant (feedforward-factor in this system is 0 mA/V[52]), avoiding complications related to the residual amplitude modulation effects.[53,54] Scanning was performed using step functions, incrementally increasing the voltage. The modulation frequency was set at f_m = 1.5 kHz, and

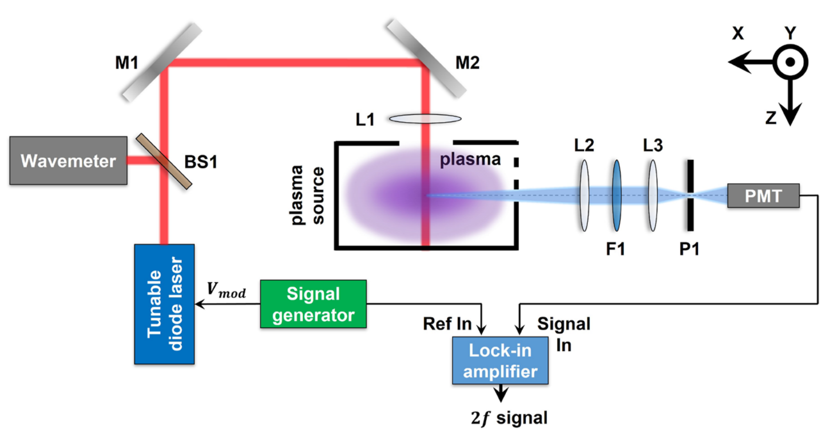

FIG. 8. Block diagram of the WM LIF setup and beam path into the plasma source. BS1—beam splitter; M1,2—mirrors; L1,2,3—lenses; P1—pinhole; F1—bandpass filter; PMT—photomultiplier tube.

a complete scan across the absorption profile took ~150 s. This laser model can accommodate modulation frequencies up to 3 kHz. The modulation depth was selected to be about a quarter of the Doppler-broadened spectral linewidth. The primary constraint on the modulation depth was ensuring the scan remained mode-hop free.

A more comprehensive description of the setup, along with its schematic, is available in Ref. 50. The AM modulation setup differed primarily by the inclusion of a mechanical chopper, which was used to modulate the laser intensity amplitude.

V. EXPERIMENTAL RESULTS AND DISCUSSIONS

Measurements were conducted at two locations (center and middle), each repeated three times. Figure 9 displays the averaged AM signals, which represent the argon IVDF profiles (red line with circles), and WM signals, which represent the second derivatives of IVDFs (blue line with squares), along with standard deviations (obtained from three measurements, shaded area). In these experiments, the true shape of the IVDFs is not known *a priori*; thus, the obtained IVDFs are first evaluated visually to assess fitting results, as presented below. At the center location [Fig. 9(a)], the IVDF features two distinct peaks, one near 0 km/s and another at −2.5 km/s. The middle location [Fig. 9(b)] shows an IVDF with a single peak at 0 km/s and asymmetrical tails in both directions, the negative being more pronounced.

To evaluate the data, AM and WM curves were fitted at each position using Eqs. (1) and (5), respectively. The laser light frequency ν was converted to velocity using Eq. (3). The number of distributions N varied from 1 to 5 to emphasize variations in fitting outcomes, and GoF was assessed using χ^2_{red}, as shown in Eq. (6). The optimal N was identified as corresponding to the minimum value ofχ^2_{red}. Note that this value differs from unity, as the obtained measurement error is overestimated as only three measurements were performed for each VDF. Figures 10 and 11 display the corresponding χ^2_{red} and VDF parameters (most probable velocity and temperature) as functions of the number of fitted distributions. Error bars were obtained as 95% confidence intervals for the nonlinear least-squares parameter estimates.

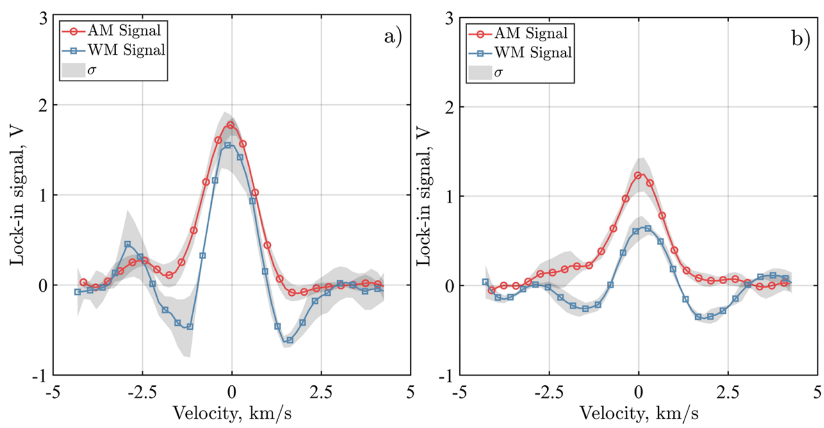

FIG. 9. Experimentally obtained AM signals or IVDF profiles (red, circles) and their WM signals, or IVDF second derivatives (blue, squares) for two locations (central and middle). The shaded area represents the standard deviation of three measurements.

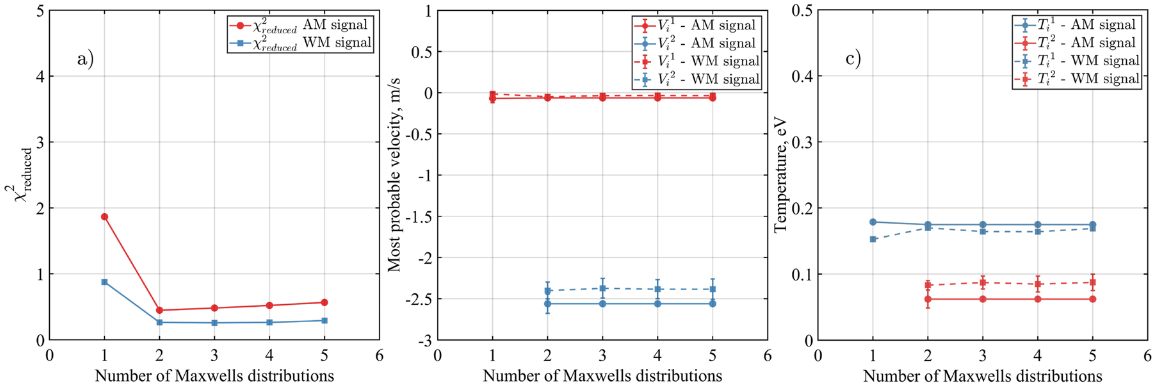

FIG. 10. (a) χ^2_{red} evolution of fitting with the number of Maxwellian distributions N; (b) most probable velocities of two main distributions; (c) temperatures of two most probable distributions.

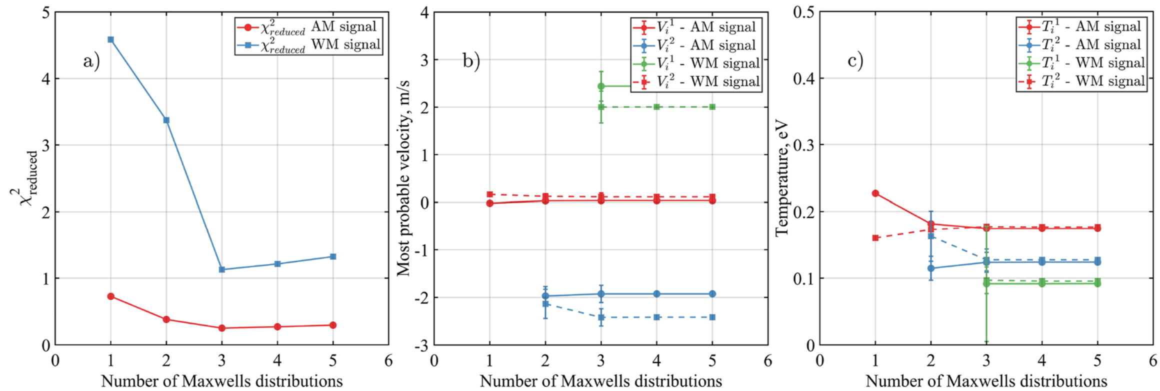

FIG. 11. (a) χ^2_{red} evolution of fitting with the number of Maxwellian distributions N; (b) most probable velocities of two main distributions; (c) temperatures of two most probable distributions.

For the central location measurements [Fig. 10(a)], the χ^2_{red} for both AM and WM signals exhibit similar trends, reaching a minimum at $N = 2$. In this case, signal noise is low, and the WM method serves as an independent verification of AM method findings, while not offering better sensitivity in terms of χ^2_{red}.

For measurements at the middle location (Fig. 11), the χ^2_{red} for both AM and WM signals shows that the optimal $N = 3$. However, variations of χ^2_{red} for WM signal are more drastic with a very pronounced minimum. This shows that the WM signal in case of stronger noise is more sensitive to fitting parameter variations. This aligns with the modeling example shown in Sec. III A, when, in case of strong noise, the AM signal can even fail to provide the correct answer. This supports the main claim of this article that the WM method is more sensitive to fitting parameters. The best-fitted curves for all cases are shown in Figs. 12 and 13.

It is essential to highlight the limitations and drawbacks of the WM technique. First, modulation parameters such as amplitude Δ and frequency ω_m [see Appendix B, Eq. (B1)] must be carefully selected. Arbitrary choices for these parameters can distort the resulting signal from the spectral line's derivative,[17,55] necessitating a rigorous signal modeling and follow up fitting process. In this work, modulation parameters were obtained empirically by varying the frequency and amplitude of a modulation. Second, when current modulation is used for wavelength modulation, the presence of residual amplitude modulation (RAM)[56] introduces nonlinear complexities to the signal. This demands either additional laser characterization,[40] more sophisticated signal fitting models,[41] or methods to mitigate this effect.[42] However, in the present work, this is not an issue, as piezo actuator voltage was modulated, which has zero feedback on the diode current, meaning that the laser power remained constant. It was experimentally verified as well, by monitoring laser power with the photodiode with and without applied modulation, see Appendix C. The reduced WM signal amplitude, as compared to the AM signal, may necessitate longer acquisition times to achieve an acceptable signal-to-noise ratio. However, even when direct AM measurements are more straightforward, WM–LIF can serve as a valuable complementary technique for verifying results.

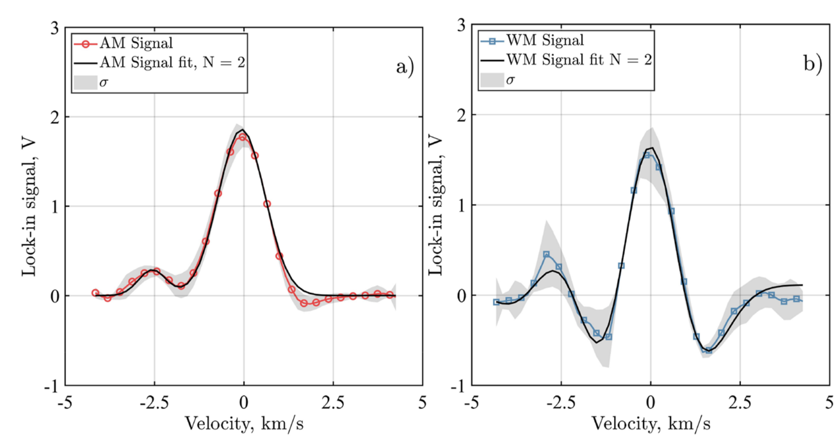

FIG. 12. Best fits of the (a) AM signal and (b) WM signal at the central location. N shows the number of the Maxwellian distribution.

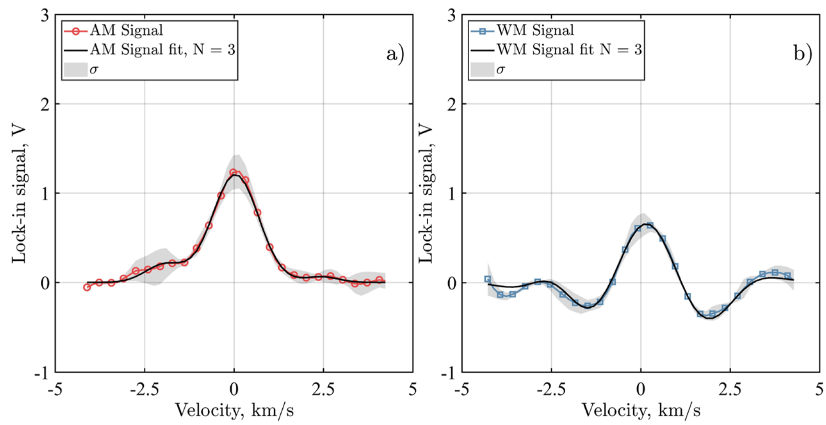

FIG. 13. Best fits of the (a) AM signal and (b) WM signal at the middle location. *N* shows the number of the Maxwellian distribution.

VI. CONCLUSION

In this paper, we explored the application of WM spectroscopy to enhance the sensitivity analysis of VDFs obtained through LIF measurements. While WM–LIF measurements have previously been conducted, this approach has not been applied to VDF measurements and analysis in plasma applications. Our modeling demonstrated that the fitting of the WM signal exhibits higher sensitivity to the true shape of VDFs compared to the AM signal. Using the χ^2_{red} as a GoF metric, the WM signal shows larger variability, contrasting with the AM signal. Fitting of the WM signal accurately predicted the correct number of distribution components, unlike fitting of the AM signal (see Fig. 5). This enhanced sensitivity is due to the derivative nature of the WM signal. Analytically, it comes from the fact that, contrary to the AM signal, the amplitude of the WM signal depends on the temperature, density, and most probable velocity of the probed distribution [see Eq. (5)].

Experimental validation was performed with measurements in argon plasma, generated by a discharge with a thermionic cathode, and applied electric and magnetic fields. The argon IVDFs and their second derivatives were examined at two distinct locations. The IVDF shapes were characterized using the same fitting process applied to the modeled signals, with the χ^2_{red} as the GoF metric. For the tested experimental conditions, both the AM and WM methods yielded similar VDF parameters, such as the most probable velocities and ion temperatures. In conditions of strong signals (center position), both AM and WM methods produced comparable results, where the WM signal served as an independent method for verifying the obtained plasma parameters. However, in scenarios with higher noise (middle position), the χ^2_{red} showed higher variability in fitting parameters for the WM signal, thereby more effectively identifying the VDF shape. This observation aligns with the results obtained for the modeled signal.

Thus, when applied with the appropriate modulation parameters, such as frequency and amplitude, WM–LIF serves multiple purposes. It offers a reliable method to verify AM LIF signals, enhancing the robustness of plasma diagnostics. Due to the derivative nature of the WM signal, it effectively cancels out strong background emissions, thus improving the dynamic range of the measurement. The increased sensitivity of WM–LIF to the shape of the VDF allows for a more precise identification of true distribution parameters, such as the number of distribution components and their characteristics. This is particularly beneficial in environments with strong noise. Overall, the introduction of WM–LIF as a tool for plasma diagnostics provides new capabilities in the analysis of complex plasma environments.

ACKNOWLEDGMENTS

This work was performed under the U.S. Department of Energy through Contract No. DE-AC02-09CH11466. The authors would like to acknowledge Nirbhav Chopra for fruitful discussions and comments on the text.

AUTHOR DECLARATIONS

Conflict of Interest

The authors have no conflicts to disclose.

Author Contributions

I. Romadanov: Conceptualization (lead); Data curation (lead); Formal analysis (lead); Investigation (lead); Methodology (equal); Software (lead); Validation (lead); Visualization (equal); Writing – original draft (lead); Writing – review & editing (equal). **Y. Raitses**: Formal analysis (equal); Funding acquisition (lead); Investigation (equal); Methodology (equal); Project administration (lead); Resources (lead); Supervision (lead); Writing – review & editing (equal). **A. Smolyakov**: Formal analysis (equal); Methodology (equal); Writing – review & editing (equal).

DATA AVAILABILITY

The data that support the findings of this study are available from the corresponding author upon reasonable request.

APPENDIX A: AM SIGNAL MODEL

The AM signal, yielding the zero-order derivative of the VDF, is obtained when the laser intensity amplitude is modulated through

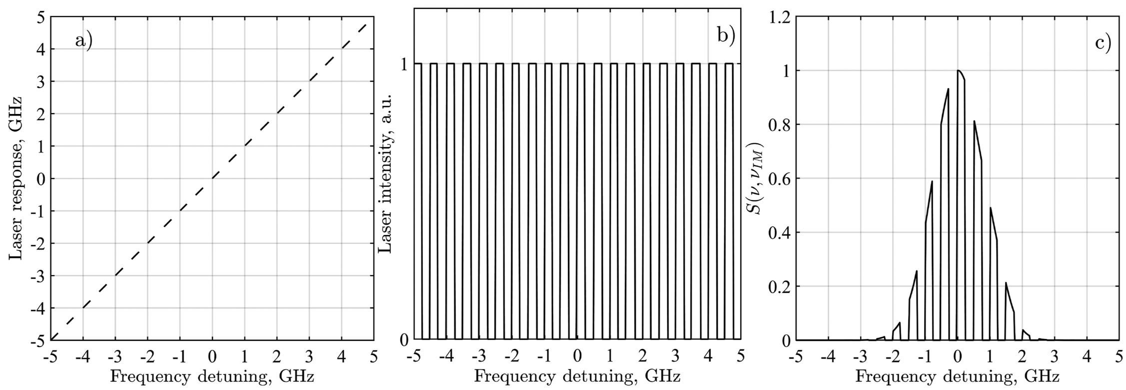

FIG. 14. (a) Laser frequency response and (b) laser intensity response in intensity amplitude modulation configuration. Line interruptions represent the zero amplitude of laser intensity. (c) $S(\nu, \nu_{AM})$ function.

variations in the laser diode current, a mechanical chopper, or an acousto-optic modulator. Concurrently, the laser's central wavelength is scanned across the absorption line. The laser response can be represented as follows:

$$\nu_{AM}(\nu) = \text{sgn}\,(A \cdot \sin(2\pi\omega_m(\nu(t) - \nu_0)) + A) \cdot (\nu(t) - \nu_0), \quad \text{(A1)}$$

where *sgn* is the sign function, returning 1, 0, or −1 depending on the sign of the input function f, A is the oscillation amplitude, $\omega_m = \omega_{ref}$ is the modulation frequency, and ν_0 is the central frequency. Note that ν is varied in time during the laser frequency scan. The laser frequency and intensity amplitude responses are illustrated in Figs. 14(a) and 14(b). For illustration purposes, an artificially low ω_m was selected. In Fig. 14(a), interruptions in line represent cases when amplitude is zero. In this case, the fluorescence signal, detected by the photodetector, can be written as [using Eqs. (1) and (2)]

$$S(\nu, \nu_{AM}) = \int f(\nu) L(\nu, \nu_{AM}) d\nu. \quad \text{(A2)}$$

The shape of the $S(\nu, \nu_{AM})$ function is illustrated in Fig. 14(c).

The lock-in amplifier signal outputs from Eq. (4) are written as

$$X_{AM} = \int_{\nu_1}^{\nu_2} S(\nu, \nu_{AM}) \sin(2\pi\omega_m \nu(t)) d\nu,$$
$$Y_{AM} = \int_{\nu_1}^{\nu_2} S(\nu, \nu_{AM}) \cos(2\pi\omega_m \nu(t)) d\nu, \quad \text{(A3)}$$

where integration is performed across the range of laser scanning frequencies, and this range is defined by the lock-in amplifier constant. The VDF, which is proportional to $S(\nu, \nu_{AM})$, can be obtained as a magnitude of the signal vector $R = \sqrt{X_{AM}^2 + Y_{AM}^2}$.

APPENDIX B: WM SIGNAL MODEL

The laser light modulation signal was modeled as a combination of a laser light frequency being scanned (linearly) across the absorption line and simultaneously being sinusoidally modulated at frequency $2\pi\omega_m$. Laser light intensity amplitude was assumed to be unaffected by modulations; see details about laser modulation

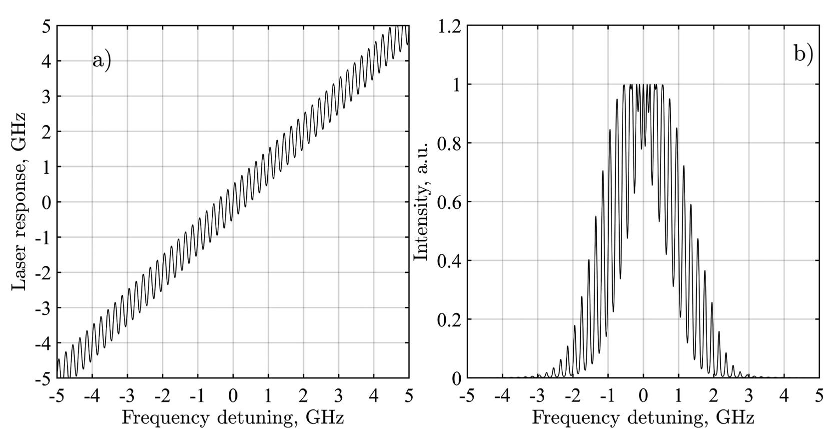

FIG. 15. (a) Laser response in WM configuration; (b) simulated WM signal $S(\nu, \nu_{WM})$ for a scan across an absorption line.

in Sec. III. According to the definition of WM, the oscillation frequency is chosen to be $\omega_m \ll \nu_0$, and the amplitude Δ is chosen to be less than the FWHM of the Doppler shifted profile.[20] To summarize all the above, the laser response in the case of the WM signal is written as

$$\nu_{WM}(\nu) = a(t)\nu(t) - \nu_0 + \Delta \sin\left(2\pi\omega_m(\nu(t) - \nu_0)\right), \tag{B1}$$

where a defines the speed of the sweeping, ν_0 is the central frequency, Δ is the modulation amplitude, and ω_m is the modulation frequency. Laser response is illustrated in Fig. 15(a).

Similar to the AM case, the signal detected by the photodetector in this case can be written as [from Eqs. (1) and (2)]

$$S(\nu, \nu_{WM}) = \int f(\nu)L(\nu, \nu_{WM})d\nu.$$

Note that an explicit analytical expression for this function is not feasible due to the integral containing a product of a Gaussian and a Lorentzian function, where the laser's central frequency in the Lorentzian function is also modulated. Therefore, we solve this equation numerically. An example of the $S(\nu, \nu_{WM})$ function is depicted in Fig. 15(b), representing the convolution of the VDF shape with the laser response function.

The lock-in amplifier signal outputs [Eq. (4)] are written as

$$\begin{aligned} X_{WM} &= \int_{\nu_1}^{\nu_2} S(\nu, \nu_{WM}) \sin\left(2\pi(2\cdot\omega_m)\nu(t)\right)d\nu, \\ Y_{WM} &= \int_{\nu_1}^{\nu_2} S(\nu, \nu_{WM}) \cos\left(2\pi(2\cdot\omega_m)\nu(t)\right)d\nu, \end{aligned} \tag{B2}$$

where integration is performed across the range of laser scanning frequencies, and this range is defined by the lock-in amplifier constant. Note that lock-in frequency is set to $2\pi(2\cdot\omega_m)$, which allows for extraction of the second derivative of the VDF shape. Similarly, in the AM case, it is possible to use the magnitude of the signal vector R; however, as it was shown in Refs. 20, Eq. (B9), the X_{WM} component is proportional to the nth derivative.

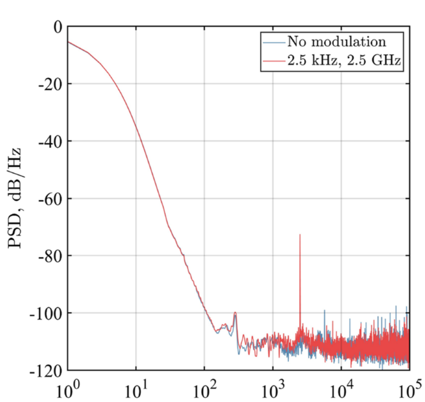

FIG. 16. PSD of PD signals with and without applied modulation to the piezo actuator driver.

APPENDIX C: MODULATION EFFECT ON LASER POWER

Measurements of the laser power were performed by integrating a beam splitter into the beam path and subsequently measuring the power of the probed beam with a photodiode. Modulations at a frequency of 2.5 kHz and an amplitude of 5 V peak-to-peak were applied to the piezo actuator driver, corresponding to a 2.5 GHz modulation of the laser wavelength. The results are depicted in Fig. 16. The PSD plot, shown in Fig. 16(b), illustrates that while the modulation is detectable, its power is $\sim 10^{-7}$ times that of the 0th harmonic; thereby, RAM effects can be considered negligible.

REFERENCES

[1] R. A. Stern and J. A. Johnson, Phys. Rev. Lett. **34**, 1548 (1975).
[2] D. N. Hill, S. Fornaca, and M. G. Wickham, Rev. Sci. Instrum. **54**, 309 (1983).
[3] G. D. Severn, X. Wang, E. Ko, and N. Hershkowitz, Phys. Rev. Lett. **90**, 145001 (2003).
[4] V. H. Chaplin, B. A. Jorns, A. Lopez Ortega, I. G. Mikellides, R. W. Conversano, R. B. Lobbia, and R. R. Hofer, J. Appl. Phys. **124**, 183302 (2018).
[5] C. V. Young, A. Lucca Fabris, N. A. MacDonald-Tenenbaum, W. A. Hargus, and M. A. Cappelli, J. Appl. Phys. **130**, 183305 (2021).
[6] C. V. Young, A. L. Fabris, N. A. MacDonald-Tenenbaum, W. A. Hargus, and M. A. Cappelli, Plasma Sources Sci. Technol. **27**, 094004 (2018).
[7] S. Jun, H. Y. Chang, and R. McWilliams, Phys. Plasmas **13**, 052512 (2006).
[8] M. C. Paul, T. E. Steinberger, E. A. M. Lister, N. I. Arnold, D. Artis, S. C. Thakur, T. Hall, S. LeBlanc, E. E. Scime, E. Thomas, and G. R. Tynan, Rev. Sci. Instrum. **92**, 013502 (2021).
[9] D. Caron, R. John, E. E. Scime, and T. E. Steinberger, J. Vac. Sci. Technol., A **41**, 033001 (2023).
[10] S. Mazouffre, Plasma Sources Sci. Technol. **22**, 013001 (2012).
[11] T. B. Smith, "Deconvolution of ion velocity distributions from laser-induced fluorescence spectra of xenon electrostatic thruster plumes," Ph.D. dissertation (University of Michigan, 2003).
[12] S. Tokuda, Y. Kawachi, M. Sasaki, H. Arakawa, K. Yamasaki, K. Terasaka, and S. Inagaki, Sci. Rep. **11**, 20810 (2021).
[13] A. K. M. M. Rahman and R. Branam, IEEE Trans. Plasma Sci. **51**, 1261 (2023).
[14] B. B. Ngom, T. B. Smith, W. Huang, and A. D. Gallimore, J. Appl. Phys. **104**, 023303 (2008).
[15] E. L. Foley and F. M. Levinton, J. Phys.: Conf. Ser. **227**, 012007 (2010).
[16] R. N. Hager and R. C. Anderson, J. Opt. Soc. Am. **60**, 1444 (1970).
[17] J. M. Supplee, E. A. Whittaker, and W. Lenth, Appl. Opt. **33**, 6294 (1994).
[18] A. Foltynowicz, W. Ma, F. M. Schmidt, and O. Axner, "Wavelength-modulated noise-immune cavity-enhanced optical heterodyne molecular spectroscopy signal line shapes in the Doppler limit," J. Opt. Soc. Am. B **26**, 1384 (2009).
[19] J. Liu, G. Zhao, W. Ma, and O. Axner, Opt. Express **29**, 42411 (2021).
[20] P. Kluczynski, J. Gustafsson, Å. M. Lindberg, and O. Axner, Spectrochim. Acta, Part B **56**, 1277 (2001).
[21] L. Zhang, G. Tian, J. Li, and B. Yu, Appl. Spectrosc. **68**, 1095 (2014).
[22] G. C. Mathews and C. S. Goldenstein, Opt. Lett. **42**, 5278 (2017).
[23] C. S. Goldenstein, V. A. Miller, and R. K. Hanson, Appl. Phys. B **120**, 185 (2015).
[24] K. A. Peterson and D. B. Oh, Opt. Lett. **24**, 667 (1999).
[25] A. Diallo, S. Keller, Y. Shi, Y. Raitses, and S. Mazouffre, Rev. Sci. Instrum. **86**, 033506 (2015).
[26] A. Heiler, R. Friedl, and U. Fantz, J. Appl. Phys. **127**, 113302 (2020).
[27] C. Lütke Stetzkamp, T. V. Tsankov, and U. Czarnetzki, J. Phys. D: Appl. Phys. **54**, 305202 (2021).
[28] J. Y. Kim, J. Y. Jang, J. Choi, J. Wang, W. I. Jeong, M. A. I. Elgarhy, G. Go, K.-J. Chung, and Y. S. Hwang, Plasma Sources Sci. Technol. **30**, 025011 (2021).
[29] A. T. Giese and C. S. French, Appl. Spectrosc. **9**, 78 (1955).
[30] V. J. Hammond and W. C. Price, J. Opt. Soc. Am. **43**, 924 (1953).

[31] L. Dixit and S. Ram, Appl. Spectrosc. Rev. **21**, 311 (1985).
[32] See https://www.thinksrs.com/downloads/pdfs/applicationnotes/AboutLIAs.pdf.
[33] C. S. Goldenstein, R. M. Spearrin, I. A. Schultz, J. B. Jeffries, and R. K. Hanson, Meas. Sci. Technol. **25**, 055101 (2014).
[34] J. Xia, F. Zhu, S. Zhang, A. Kolomenskii, J. Dong, K. Okada, J. Strohaber, and H. A. Schuessler, Opt. Lasers Eng. **117**, 21 (2019).
[35] T. R. S. Hayden, N. Malarich, D. Petrykowski, S. P. Nigam, J. D. Christopher, C. Lapointe, N. T. Wimer, P. E. Hamlington, and G. B. Rieker, Appl. Phys. B **125**, 226 (2019).
[36] J. Reid and D. Labrie, Appl. Phys. B **26**, 203 (1981).
[37] H. Li, G. B. Rieker, X. Liu, J. B. Jeffries, and R. K. Hanson, Appl. Opt. **45**, 1052 (2006).
[38] G. C. Bjorklund, M. D. Levenson, W. Lenth, and C. Ortiz, Appl. Phys. B **32**, 145 (1983).
[39] C. Durot, B. A. Jorns, E. Dale, and A. D. Gallimore, *Laser-Induced Fluorescence Measurement of the Anomalous Collision Frequency in a 9-kW Magnetically-Shielded Hall Thruster* (Georgia Institute of Technology, Atlanta, Georgia, 2017).
[40] S. M. Penn, J. P. M. Beijers, R. A. Dressler, V. M. Bierbaum, and S. R. Leone, J. Chem. Phys. **93**, 5118 (1990).
[41] N. R. Walkden, A. Wynn, F. Militello, B. Lipschultz, G. Matthews, C. Guillemaut, J. Harrison, D. Moulton, and J. E. T. Contributors, Nucl. Fusion **57**, 036016 (2017).
[42] K. Banaszek and K. Wódkiewicz, Phys. Rev. A **55**, 3117 (1997).
[43] K. G. Libbrecht, E. D. Black, and C. M. Hirata, Am. J. Phys. **71**, 1208 (2003).
[44] W. Huang, T. Smith, and A. Gallimore, in *40th AIAA Plasmadynamics And Lasers Conference* (American Institute of Aeronautics and Astronautics, San Antonio, TX, 2009).
[45] E. Pawelec, S. Mazouffre, and N. Sadeghi, Spectrochim. Acta, Part B **66**, 470 (2011).
[46] W. A. Hargus, G. M. Azarnia, and M. R. Nakles, Rev. Sci. Instrum. **83**, 103111 (2012).
[47] P. Svarnas, I. Romadanov, A. Diallo, and Y. Raitses, IEEE Trans. Plasma Sci. **46**, 3998 (2018).
[48] A. Lucca Fabris, C. V. Young, and M. A. Cappelli, J. Appl. Phys. **118**, 233301 (2015).
[49] I. A. Biloiu and E. E. Scime, Phys. Plasmas **17**, 113509 (2010).
[50] I. Romadanov and Y. Raitses, Rev. Sci. Instrum. **94**, 073002 (2023).
[51] V. Skoutnev, P. Dourbal, E. Rodríguez, and Y. Raitses, Rev. Sci. Instrum. **89**, 123501 (2018).
[52] I. Romadanov, Email to a Service Representative, 2024.
[53] P. Kluczynski, Å. M. Lindberg, and O. Axner, Appl. Opt. **40**, 783 (2001).
[54] P. Kluczynski, Å. M. Lindberg, and O. Axner, Appl. Opt. **40**, 794 (2001).
[55] D. G. Cameron and D. J. Moffatt, Appl. Spectrosc. **41**, 539 (1987).
[56] E. A. Whittaker, M. Gehrtz, and G. C. Bjorklund, J. Opt. Soc. Am. B **2**, 1320 (1985).